Check for updates

ADVANCED OPTICAL MATERIALS
www.advopticalmat.de

Enhanced Interlayer Interaction in Top-Layer Twisted Trilayer MoS_2 with Moiré Superlattice

Yalin Liu, Tiantian Zhang, Jun Zhou, Meijie Zhu, Zihan Zhao, Weifeng Zhang, Yibiao Feng, Xiaopeng Guo, Nan Liu, Jiacai Nie, Shanshan Chen, and Ruifen Dou**

Moiré superlattices, induced by an angular mismatch in layered materials provide a new index of freedom to manipulate the correlated electron states and many-body properties of excitons. Here, trilayer MoS_2 homostructures with the 3R configuration between the middle (M) and the bottom (B) layer and the top-to-middle (T-M) interlayer twists ranging from 10° to 40° are fabricated via NaCl-assisted chemical vapor deposition. The twist-dependent interlayer interactions are systematically investigated by polarized low frequency (PLF) and high frequency (HF) Raman spectroscopy. PLF Raman results show that the energy shift in the shear mode, the breathing modes of LB_{31} and LB_{32} is respectively the much in 14°- and 28°-T-M twisted trilayer, among as-prepared trilayer MoS_2 homostructures. Moreover, the T-M twist further affects the optical properties of the twisted MoS_2 trilayer, evidenced by the photoluminescence (PL) spectroscopy. Moiré excitons are enhanced in the top-layer twisted MoS_2 trilayer with a T-M twists of 28°, which may originate from the interlayer exciton trapped by the periodical moiré potential. The present work demonstrates that the trilayer homostructures tuned by interlayer twists can be an ideal system to tune the energy band structures and exciton properties for their potential applications in the nano-optical electronics.

1. Introduction

Moiré superlattices, formed through vertical stacking two layers of 2D materials with different lattice constants or with a small twist angle, generally engender interlayer momentum mismatch and thus lead to a mini moiré Brillouin Zone.[1–7] Therefore, moiré superlattices provide a novel and attainable platform to engineer the energy band structures and correlated electronic properties owing to the electron confinement from the periodical moiré superlattices.[8,9] It has been reported that unconventional superconductivity and Mott insulating states are observed in "magic-angle" twisted bilayer graphene.[3–7] Analogous to the graphene-based moiré superlattice, twisted bilayer heterostructures and homostructures comprised of transition metal dichalcogenides (TMDs) further exhibit ultraflat bands in the low energy regime, giving rise to strong correlated physics at small twist angles.[2,10–19] Besides, for TMD-based twisted bilayer heterostructures with relative small twist angles (<2°), periodical moiré patterns also offer new possibilities to probe novel optoelectronic excitations such as moiré excitons.[20–26] It was initially reported that moiré excitons were interlayer excitons composed of electrons and holes belonging to different layers, which are trapped by periodically moiré potentials in the type-II band-aligned heterostructures.[27] The intrinsic nature of moiré excitons originating from the internal spatial electron-hole correlations can be held in the moiré superlattices.[28,29] Very recently, both theoretical and experimental works show that the origin of moiré excitons confined by the moiré superlattice may be the modulated intralayer Wannier excitons.[23,30] This means that the strong hybridization from interlayer and intralayer excitons can be generated in twisted heterobilayers and homobilayers.[18,23,31]

Except for the TMD-based moiré superlattices with a small twist angle, the intense moiré exciton peaks appear in the bilayer MoS_2 with larger interlayer twists of 21.8° and 27.8° defined as the commensurate angle, which predominantly result from the miniband in refolded Brillouin zones.[22] Theoretical calculations also predict that the TMD-based moiré superlattices with a commensurate angle may host ultraflat energy bands, thus leading to the correlated electron states and moiré excitons phenomena.[14] This implies that the properties of moiré excitons in the twisted homobilayers might be more complex due to both hybridization and moiré superlattice potentials highly correlated to the lattice reconstruction over a range of twist angles as well as the

Y. Liu, T. Zhang, J. Zhou, Y. Feng, X. Guo, J. Nie, R. Dou
Department of Physics
Beijing Normal University
Beijing 100875, P. R. China
E-mail: rfdou@bnu.edu.cn
M. Zhu, S. Chen
Department of Physics
Renmin University of China
Beijing 100872, P. R. China
E-mail: schen@ruc.edu.cn
Z. Zhao, W. Zhang, N. Liu
Beijing Key Laboratory of Energy Conversion and Storage Materials
College of Chemistry
Beijing Normal University
Beijing 100875, China

The ORCID identification number(s) for the author(s) of this article can be found under https://doi.org/10.1002/adom.202400907

DOI: 10.1002/adom.202400907

 © 2024 Wiley-VCH GmbH

interlayer distance.[2,5,7,16,32,33] However, to date, the deep investigation of moiré excitons in homobilayer system is still less due to the difficult in precisely fabrication of twisted homostructure with a clean interface and the strong interlayer interaction. More importantly, twisted trilayer system exhibits similar properties as those of the bilayer structures, such as the strong electron correlated states found in twisted trilayer graphene structure.[34] Therefore, controllable preparation of twisted TMD-based homotrilayer with versatile interlayer twists is a prerequisite for regulating the interlayer interaction strongly coupled to moiré superlattices and thus modulating their exotic correlated electronic properties and exciton-related many-body properties.

In this contribution, trilayer MoS_2 homostructures with the 3R (twist angle of 0°) stacking configuration from the bottom to the middle layer and the top-to-middle (T-M) interlayer twists ranging from 10° to 40° were fabricated by design via NaCl-assisted chemical vapor deposition (CVD). The twist-dependent interlayer interactions are systematically investigated by polarized low frequency (PLF) and high frequency (HF) Raman spectroscopy. PLF Raman results show that peak positions of the shear mode of S_{31}, the breathing modes of LB_{31} and LB_{32}, representing the trilayer interlayer interaction, are red-shift in the top-layer twisted trilayer (tT) MoS_2 superstructures with a non-zero T-M twist, compared to the top-layer tT MoS_2 with a 0° (60°) T-M interlayer twist. Moreover, the energy shift of the shear mode of S_{31} and the breathing modes of LB_{32} and LB_{31} are the largest for the 28°-T-M tT MoS_2 and the 14°-T-M tT MoS_2, respectively, which means that interlayer coupling for the tT MoS_2 system at a special interlayer twist, approaching to the commensurate angle, can be enhanced by the periodical moiré potential. The T-M twist further affects the many-body exciton complexes in the tT MoS_2, which are rationally evidenced via the room-temperature and variable temperature photoluminescence (PL) spectroscopy. Our PL results demonstrate that the indirect energy gap is gradually expanded with the T-M twist closing to about 30°. Moreover, moiré excitons were observed in the top-layer tT MoS_2 with the commensurate T-M twists of 14° and 28° and enhanced in the top-layer tT MoS_2 homostructures with a special twist of approximate 28°, which is owing to the interlayer excitons confined by the corresponding periodical moiré potential. The present work demonstrates that trilayer homostructures tuned by interlayer twists might be an ideal system to explore the energy band structures and exciton properties for their potential applications in the nano-optical electronics.

2. Results and Discussion

2.1. Raman Measurement of Top-Layer Twisted Trilayer MoS_2

Figure 1a shows representative optical microscope images of the trilayer MoS_2 with different top-to-middle (T-M) interlayer twists of about 0°, 60°, 14°, 28° and 30°. More optical microscope images of bilayer and top-layer tT MoS_2 could be seen in Figure S1 (Supporting Information). The top-layer tT structures are fabricated through irregular changing the substrate temperature and the carrier gas (Ar) flow, which means that the growth equilibrium process is no longer continuous so as to form the energetically metal-stable stacked bilayer and trilayer patterns with interlayer twists between the top, the middle and the bottom layer. The detailed growth process is schematically described in Figure S2 (Supporting Information) and the growth mechanism of the top-layer tT MoS_2 homostructures will be discussed elsewhere. Here, we can clearly discern the different layers of twisted MoS_2 trilayer based on the color contrast in Figure 1a, as highlighted by the black, blue and yellow dashed lines correspondingly drawing the contours of the bottom, middle and top layer, respectively. The T-M interlayer twist angle (θ_{T-M}) is determined by the relative rotation angle between two vertically stacked triangles, as shown by the rotation angle of dashed lines of the top and the middle triangle in the right panel of Figure 1a. Under this definition, the deviation of twist angles is normally ± 1°. The bottom-to-middle (B-M) interlayer twist angle is defined as θ_{B-M}, similar to that of θ_{T-M} shown in Figure S1j (Supporting Information).

To investigate the evolution of phonon vibrations and interlayer coupling in twisted MoS_2 trilayer, the low-frequency (LF) Raman spectra were obtained in tT MoS_2 homostructures with a 3R stacking in B-M and T-M interlayer configuration (θ_{B-M} = 0°, θ_{T-M} = 0°) (named as 3R-3R) in Figure 1b. For comparing the Raman results from the bilayer and trilayer MoS_2 homostructures, Raman spectroscopy studies are carried out in bilayer MoS_2 with 3R and 2H (twist angle of 60°) stacking forms and trilayer MoS_2 with 3R-3R, 2H-3R, 3R-2H and 2H-2H are shown in Figures S3 and S4 (Supporting Information), respectively. Herein, a dark blue line in Figure 1b displays a shear (S) mode S_{32} at 16.40 cm^{-1} and a LF breathing mode (LB_{32}) at 28.17 cm^{-1}, similar to the former study on the trilayer MoS_2 with a 3R stacking structure.[35–37] The parallel and the vertically polarized Raman spectroscopy was performed to distinguish the difference in the shear mode and the breathing mode. Generally, the parallel polarized LF Raman spectrum contains the parallel components of the shear mode and the breathing mode, whilst the vertical component of the shear mode can be only detected by the vertical polarized LF Raman spectrum.[35,36,38–40] The red curve representing the parallel polarized LF Raman spectrum in Figure 1b shows two peaks, respectively, corresponding to S_{32} mode at 16.40 cm^{-1} and LB_{32} mode at 28.17 cm^{-1}. The blue curve of the vertical polarization Raman spectrum displays one peak, protruding at 16.40 cm^{-1}, which contains only the vertical component of S_{32} modes. To explore the layer number effect on Raman vibration modes, Raman measurements were further performed for the 3R stacking bilayer MoS_2, as shown by the green curve in Figure 1b. This curve displays a shear (S_{21}) mode at 22.87 cm^{-1} and a LF breathing (LB_{21}) mode at 39.08 cm^{-1}.[41] The parallel polarized LF Raman spectrum represented by the purple curve from the 3R bilayer MoS_2 shows a S_{21} mode at 22.87 cm^{-1} and a LB_{21} mode at 39.08 cm^{-1}. The yellow curve from the vertical polarized LF Raman spectrum only displays one peak, corresponding to vertical component of the S_{21} shear mode at 22.87 cm^{-1}. Figure 1b clearly shows a red shift of the shear mode (S_{32}, 16.40 cm^{-1}) of the trilayer MoS_2 with the 3R-3R stacking mode, comparing with that (S_{21}, 22.87 cm^{-1}) of the 3R stacking bilayer MoS_2. Meanwhile, a new breathing mode of LB_{32} at 28.17 cm^{-1} appears in 3R-3R stacking trilayer MoS_2, which is not present in the 3R stacking bilayer MoS_2. The difference of Raman vibration in trilayer and bilayer MoS_2 is rationale because of the LF Raman phonon modes determined by the interlayer van der Waals interaction highly sensitive to the layer numbers.

© 2024 Wiley-VCH GmbH

21951071, 0, Downloaded from https://onlinelibrary.wiley.com/doi/10.1002/adom.202400907 by Beijing Normal University, Wiley Online Library on [25/06/2024]. See the Terms and Conditions (https://onlinelibrary.wiley.com/terms-and-conditions) on Wiley Online Library for rules of use; OA articles are governed by the applicable Creative Commons License

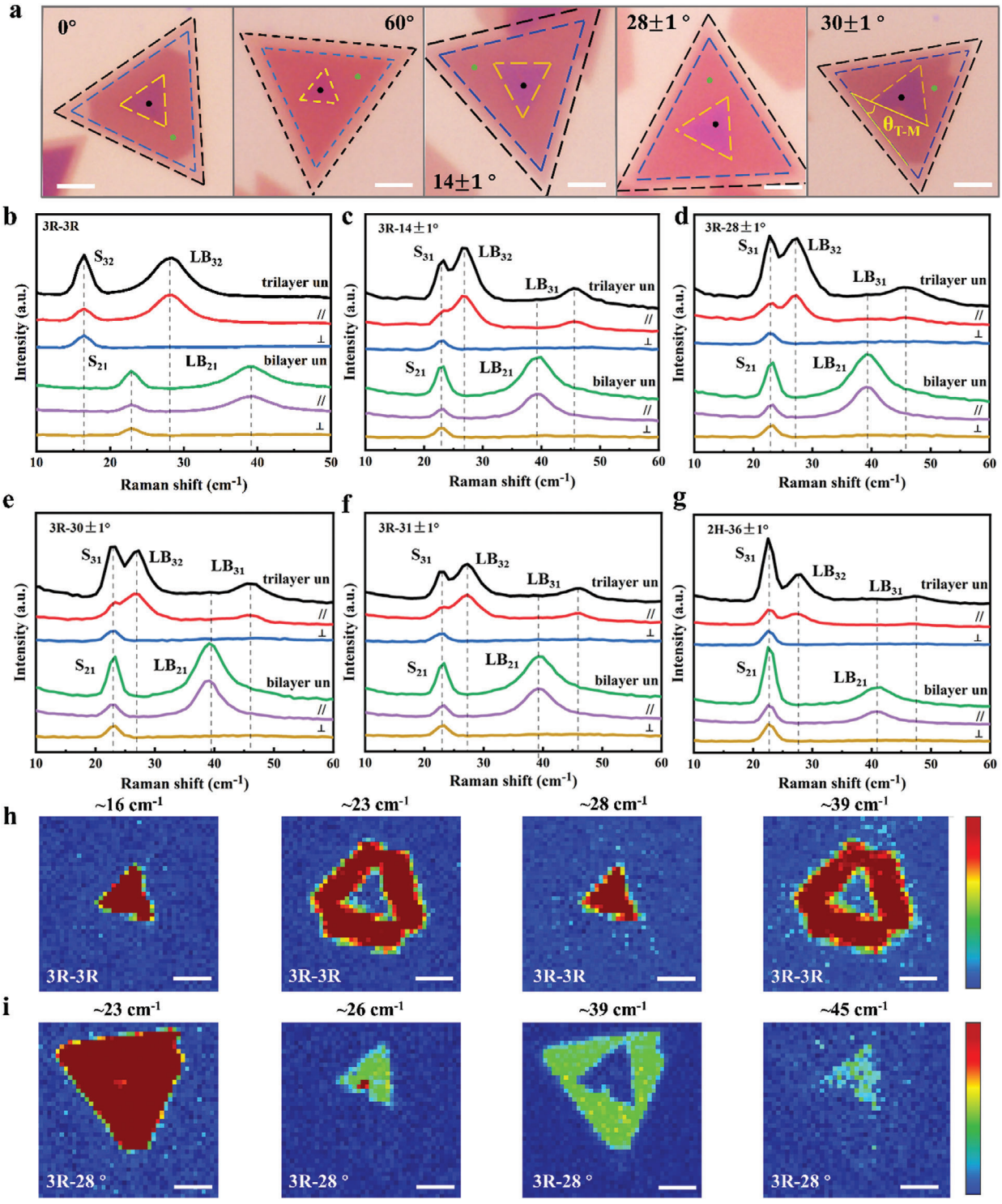

Figure 1. Optical microscope and Raman spectroscopy study of the twisted trilayer MoS_2. a) Optical microscope images of the trilayer MoS_2 with different top-to-middle (T-M) interlayer twists of about 0°(3R), 60°(2H), 14°, 28° and 30°. The scale bar in (a) is 5 μm. b) Unpolarized low-frequency Raman spectra (the black line) and vertical (the blue line) polarized Raman spectra, as well as corresponding unpolarized Raman spectra (the green line), parallel (the purple line) and vertical (the yellow line) polarized Raman spectra from the bottom bilayer of trilayer MoS_2 of 3R-3R. c–g) Unpolarized low-frequency Raman spectra (the black line), parallel (the red line), and vertical (the blue line) polarized Raman spectra, and corresponding unpolarized Raman spectra (the green line), parallel (the purple line) and vertical (the yellow line) polarized Raman spectra from the bottom bilayer of trilayer MoS_2 with the 3R bottom-to-middle (B-M) configuration and top-to-middle (T-M) twists of 14°, 28°, 29°, 31°, and the 2H B-M configuration and T-M twist of 36°. The different colored dots in (a) display Raman measurement locations for bilayer and trilayer MoS_2. h,i) Low-frequency Raman intensity mapping images from 3R-3R-1/2 and 3R-28° trilayer MoS_2 samples, respectively, obtained at different frequencies as shown on top of the image. The scale bar in (h,i) is 2 μm.

© 2024 Wiley-VCH GmbH

21951071, 0, Downloaded from https://onlinelibrary.wiley.com/doi/10.1002/adom.202400907 by Beijing Normal University, Wiley Online Library on [25/06/2024]. See the Terms and Conditions (https://onlinelibrary.wiley.com/terms-and-conditions) on Wiley Online Library for rules of use; OA articles are governed by the applicable Creative Commons License

Due to breaking the lattice symmetry caused by the introduction of the T-M interlayer twist and thus the variation in stacking configurations in trilayer MoS_2,[35] the Raman vibration modes of top-layer tT MoS_2 homostructures characterized with stacking configurations of 3R-14°, 3R-28°, 3R-30°, 3R-31°, and 3R-36° exhibit different traits in Raman modes depending on T-M interlayer twists, as depicted in Figure 1c–g. Here, the abbreviation of 3R-θ_{T-M} means a 3R stacking configuration from the bottom to the middle layer and a top layer twisted angle of θ in the tT MoS_2 homostructure. Obviously, the black curve representing the LF Raman spectrum for the as-grown top-layer tT MoS_2 with the configurations of 3R-14°, 3R-28°, 3R-30°, 3R-31°, and 3R-36° shows three peaks, which can be respectively attributed to a shear mode S_{31} and two breathing modes of LB_{31} and LB_{32} from the left to the right. The parallel (the red line) and the vertical (the blue line) polarization LF Raman in Figure 1c–g further confirm the energy positions of the shear mode and two breathing modes, similar as the analysis of Figure 1b. The comparable LF Raman spectra of bilayer MoS_2 (the green, the purple and the yellow curves) from the green dot in corresponding top-layer tT trilayer samples are provided in Figure 1c–g. Moreover, LF Raman mapping images obtained at the respective vibration frequency of the shear mode and the breathing mode (Figure 1h,i; Figure S5a–d, Supporting Information) distinctly discern the top and middle layer and further evidence the high-quality and homogeneous performance of the whole twisted trilayer MoS_2 homostructures.

For probing into the phonon mode evolution with the variation in T-M interlayer twists, the LF Raman spectra from different top-layer tT MoS_2 samples are put together in **Figure 2a**. Meanwhile, the peak positions of the shear mode and two breathing modes are summarized in Table S1 (Supporting Information). We can see that the S_{31} mode from the trilayer MoS_2 with T-M twists of 13°, 14°, 28°, 30°, and 31°display almost the similar frequency of about 23 cm^{-1} as shown in Figure 2b. Moreover, the S_{31} mode at 23 cm^{-1} is in red-shift and far away from that (16.40 cm^{-1}) of trilayer MoS_2 with a twist angle of 0° and 60°, as shown in Figure 2a. As for two breathing modes, LB_{31} and LB_{32} is in red shift of about 4.5 cm^{-1} (Figure 2c) and is about 1 cm^{-1} (Figure 2d) for the 14° and 13°-tT MoS_2, respectively. The red-shift energies of the LB_{31} and LB_{32} modes are the great for the 14°-tT MoS_2 homostructure, compared to those of other as-prepared tT MoS_2 homostructures. Similar phenomenon exists in the sample of 13°-tT MoS_2 due to the very close twist angle to 14°. Raman vibration modes are strongly sensitive to the stacking configurations. A slight deviation in atom registrations in trilayer homostructures results in different Raman vibration modes, as shown in Figure 2f,g, respectively corresponding to four different stacking forms of 3R-3R-1/2, 3R-3R-3/4 (Figure S6a–d, Supporting Information). Figure 2f,g apparently indicate the generation or annihilation in the phonon vibration modes depending on different atom registrations. Figure 2h,i describe the phone vibration modes of 3R-2H and 2H-2H. Therefore, the phonon vibration, directly revealing the interlayer interaction, can be obviously adjusted by the introduction of the twist angle in trilayer MoS_2. LF Raman spectra related to the T-M interlayer twists are summarized in Figure 2e, which tells that the interlayer interaction can be strongly tuned by the twisted top layer in MoS_2 trilayer. With the T-M interlayer twist increasing from 0° to 13°, 14°, 28°, 30° and 31°, the interlayer distance is gradually expanded and the lattice mismatch between the top and the middle layer is generated, resulting in peak positions of the shear mode approaching to that of 3R bilayer MoS_2 and thus the interlayer decoupling for samples of 3R-30° and 3R-31° tT MoS_2.

In addition to LF Raman vibrations tuned by the T-M interlayer twist and thus the interlayer coupling, the high frequency (HF) Raman spectroscopy further manifests the evolution of phonon vibrations in tT MoS_2 with the variation of the T-M interlayer twist. **Figure 3a** shows a series of HF Raman spectra from 3R bilayer MoS_2 and tT MoS_2 homostructures with a θ_{T-M} twist of 0°, 13°, 14°, 28°, 30°, 31° and 60°. Obviously, two prominent peaks located at around 382 cm^{-1} and 404 cm^{-1} are observed, being assigned to the in-plane E^1_{2g} and out-of-plane A_{1g} phonon modes, respectively. Herein, the E^1_{2g} mode for the as-grown samples of 13°-, 14°-, 28°-, 30°-, and 31°-tT MoS_2 remains unchangeable with the introduction of the T-M twist angles, comparing to that of 0° (60°)-twisted trilayer MoS_2.[25] However, the A_{1g} mode clearly displays a twist angle-dependent redshift, as shown in Figure 3b. The energy of two vibration modes in HF Raman spectra are summarized in Table S1 (Supporting Information). The twist angle-dependent A_{1g} mode is mainly determined by long-range Coulombic interlayer interactions and interlayer van der Waals interaction, respectively.[26] Therefore, the energy difference between the E^1_{2g} mode and the A_{1g} mode ($\Delta\omega = \omega_A$-ω_E) may characterize the interlayer interaction, namely, the stronger interlayer coupling generally corresponds to the greater energy difference. In the present case, the energy difference between two HF Raman peaks ($\Delta\omega$) in trilayer MoS_2 structures with a T-M twist of about 14° and 28° is a bit greater than that of other samples of 30°-, and 31°-trilayer MoS_2, which is close to that of 0°- and 60°-MoS_2 trilayer, as shown in Figure 3c. This means that the T-M interlayer coupling for samples of 14°- and 28°- is stronger than that of trilayer MoS_2 with a T-M twist angle of 30° and 31°. Moreover, the interlayer coupling is gradually weakened with the T-M twist angle approaching to 30°. Besides, the moiré phonon mode located at 407 cm^{-1}, is related to the A_{1g} phonon branch (FA_{1g}) and visible in HF Raman curves for 13°-, 14°-, 28°-, 30°- and 31°-twisted trilayer MoS_2 patterns in Figure 3a, originating from the off-center phonons of the monolayer linked with the lattice vectors of moiré reciprocal space.[23,31]

Figure 3b further shows that FA_{1g} peaks exhibit a sine-like behavior related to a T-M twist angles, in agreement with the previous studies on moiré phonon.[14,37,42] It is worth noting that the peak energy of the FA_{1g} moiré phonon is increased in the twisted trilayer MoS_2 with a $\theta_{T\text{-}M}$ of 14°, which might be due to the phonon energy matching well the potential energy of moiré superlattices. The moiré phonons in the moiré superlattices with the different twists stem from diverse wave vectors of phonon dispersion, which provides an effective way to manipulate the phonon dispersion, further generating the phonon-assisted electron excited states in K space and energy band structures.

2.2. Special Optical Properties of Top-Layer Twisted Trilayer MoS_2

We investigate the energy band structures and the excitonic properties of tT MoS_2 patterns via room-temperature (RT) and low-temperature PL spectroscopy. **Figure 4a** shows a serial of RT PL spectra of tT MoS_2 patterns with various T-M twist

© 2024 Wiley-VCH GmbH

21951071, 0, Downloaded from https://onlinelibrary.wiley.com/doi/10.1002/adom.202400907 by Beijing Normal University, Wiley Online Library on [25/06/2024]. See the Terms and Conditions (https://onlinelibrary.wiley.com/terms-and-conditions) on Wiley Online Library for rules of use; OA articles are governed by the applicable Creative Commons License

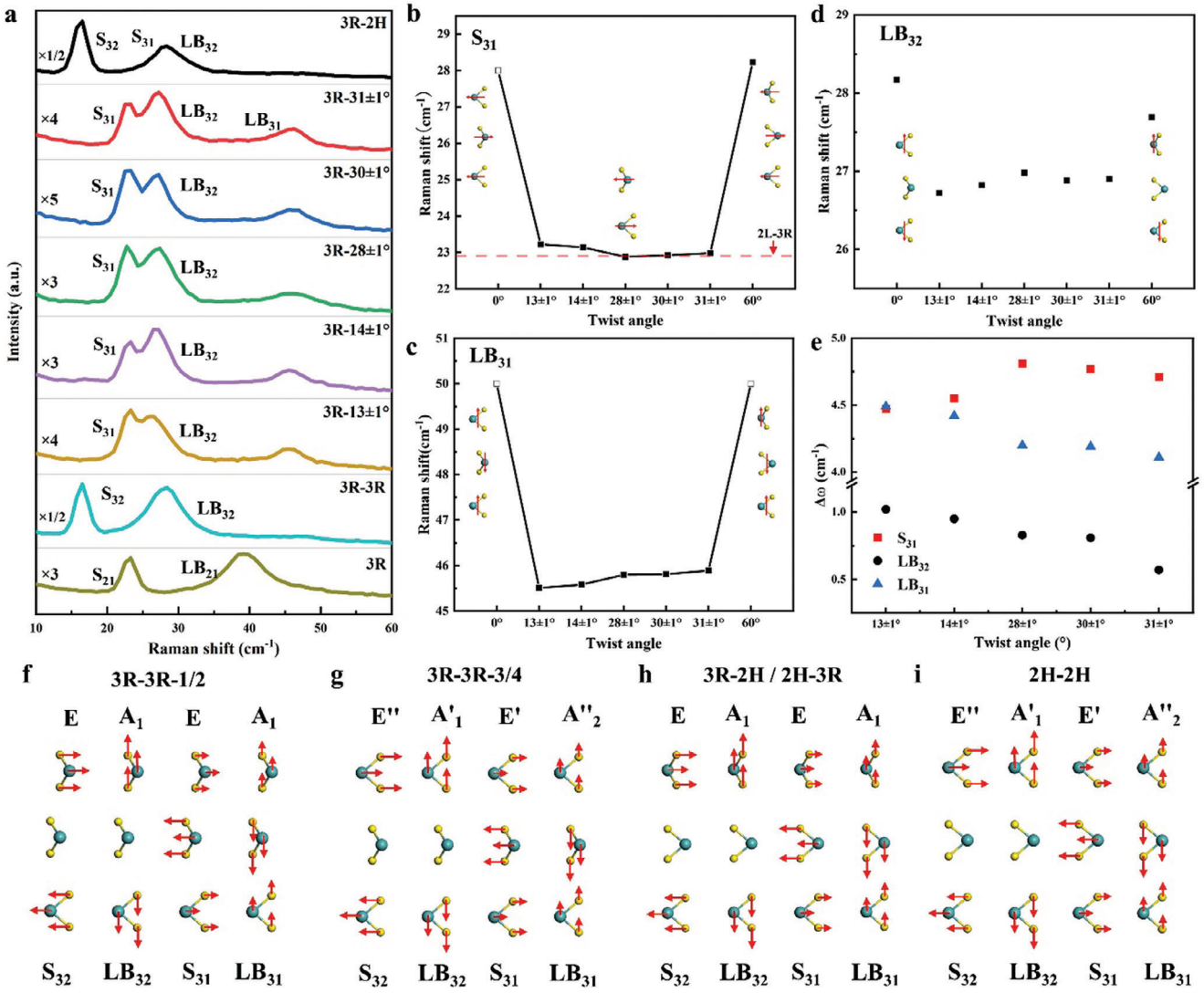

Figure 2. Low-frequency Raman characterization of the twisted trilayer MoS_2 and 3R bilayer MoS_2. a) Low-frequency Raman spectra from trilayer MoS_2 homostructures with 3R configuration in B-M interlayer and T-M twist angles of 0°, 13°, 14°, 28°, 30°, 31° and 60° and bilayer MoS_2 with 3R configuration. b–d) Peak position of S_{31}, LB_{31} and LB_{32} in LF Raman spectra of tT MoS_2 homostructures with a twisted top layer. The red dashed line in (b) represents the peak position of S_{21} of MoS_2 bilayer with a 3R configuration. e) The variation of peak positions of S_{31}, LB_{31} and LB_{32} in tT MoS_2 homostructures relative to the trilayer MoS_2 with a 0° T-M interlayer twist. f–i) The schematics and the corresponding shear mode and breathing mode of trilayer MoS_2 with different stacking configurations of (f) 3R-3R-1/2, (j) 3R-3R-3/4, (h) 3R-2H/2H-3R and (i) 2H-2H configuration.

angles on SiO_2/Si surface. The RT PL spectra of the black curve obtained at the 0°-twisted trilayer MoS_2 pattern show three prominent peaks with the positions located at around 1.819 eV, 1.939 eV, and 1.316 eV, respectively.[43] The PL peak energy at 1.819 eV originates from the oscillation of the A excitons (X^A), which is caused by the bound electron-hole pairs due to the strong Coulomb interaction in TMD semiconductors. The peak at 1.95 eV is the energy location of the B exciton (X^B), generated by the spin-orbital splitting in K space. In addition, the lower energy peak at 1.316 eV can be attributed to the indirect excitons (X^I) from the different layers,[43] occurring due to indirect momentum Q-K transition corresponding to the top of the valence band and the bottom of the conduction band. The typical schematic image of the X^A exciton, X^B exciton and (X^I) exciton radiative transition is shown in Figure S7 (Supporting Information).

Remarkably, Figure 4a shows the energy evolution of X^I with the variation in twist angles. With increasing the T-M twist angles from 0° to 30°, the low energy peak energy of X^I (in Figure 4a) is gradually enlarged from 1.316 to 1.388 eV and the corresponding peak intensity is strengthened as well. However, the peak energy of X^I is reduced from 1.388 to 1.360 eV with the T-M twist changing from 30° to 60°. The energy variation of X^I with the T-M twist angles is displayed in Table S2 (Supporting Information) in SI, which directly demonstrates that the electron band structures can be tuned by different moiré superlattices with consideration of the interlayer interaction. It is well-known that the weakened interlayer coupling in TMD-based moiré superlattices would

© 2024 Wiley-VCH GmbH

21951071, 0, Downloaded from https://onlinelibrary.wiley.com/doi/10.1002/adom.202400907 by Beijing Normal University, Wiley Online Library on [25/06/2024]. See the Terms and Conditions (https://onlinelibrary.wiley.com/terms-and-conditions) on Wiley Online Library for rules of use; OA articles are governed by the applicable Creative Commons License

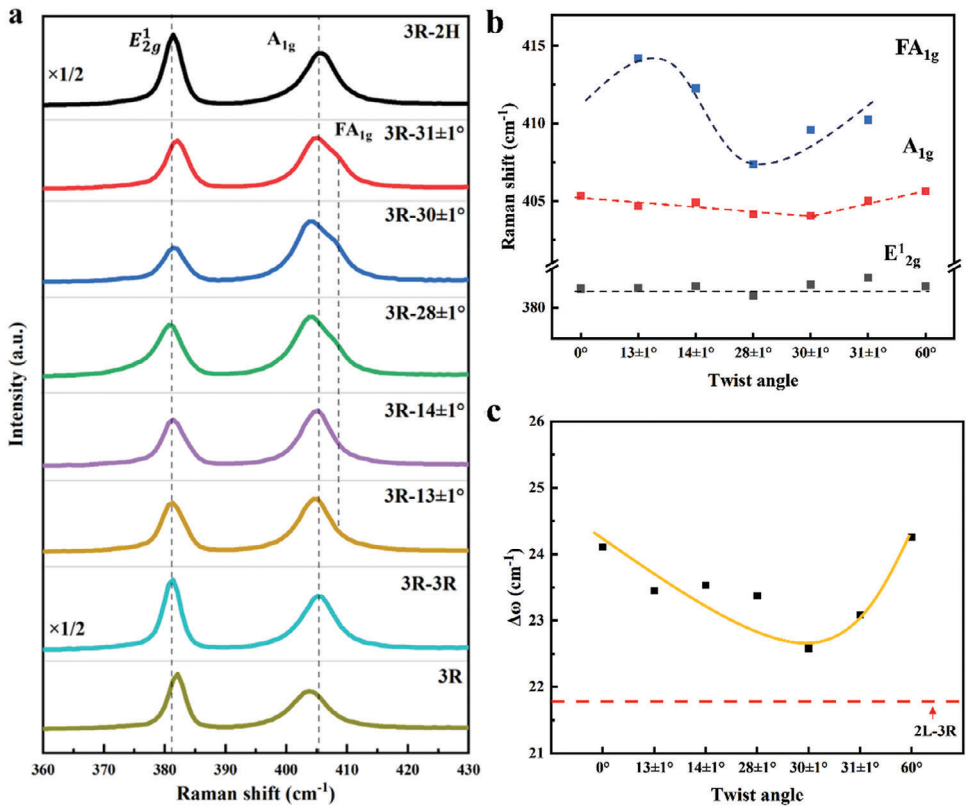

Figure 3. High-frequency Raman characterization of the twisted trilayer MoS_2 and 3R bilayer MoS_2. a) HF Raman spectra of twisted trilayer MoS_2 samples with a B-M 3R configuration and T-M twist angles from 0°, 13°, 14°, 28°, 30°, 31°, to 60°. b) The energy position of the E^1_{2g}, the A_{1g}, and the FA_{1g} Raman modes as a function of a T-M twist angle, dash lines are from the linear (E^1_{2g}, A_{1g}) and sinusoidal (FA_{1g}) fitting. c) The energy difference between A_{1g} and E^1_{2g} ($\Delta\omega$) as a function of the T-M twist angles, the red dashed line represents the frequency difference between the A_{1g} and the E^1_{2g} modes of 3R bilayer MoS_2.

result in a decrease in the bandgap at Γ point in K space, causing an enlarged indirect band gap. The indirect band gap is increased to the most value in top-layer tT MoS_2 homostructures with a twist angle of 30°, meaning the weak interlayer coupling in the 30°-tT-MoS_2. The results are in good agreement with the previous PL results[14] on increasing an indirect band gap in the bilayer MoS_2 with a 30° twist. Besides, Figure 4a shows that the energy of the X^A exciton at 1.830–1.837 eV (X^A) (see Table S2, Supporting Information) from the twisted trilayer homostructures are greater than that (1.819 eV, the black line) of the untwisted trilayer samples. The exciton at 1.931–1.940 eV (X^B) is unsensitive to T-M twist angles for the tT MoS_2 homostructures, compared to that of the untwisted trilayer homostructures. It is accepted that[14] the primary exciton peaks originate from intralayer scattering, so their energies are independent of the twist angles. Meanwhile, the X^A exciton peak broadening is more remarkable in some special twisted homostructures including 14°-, 20°-, and 28°-tT MoS_2. The energy blue shift and the broader peak in the X^A exciton can be ascribed to the interlayer coupling impacted by the periodical commensurate structure induced by the high commensurate angles such as 15.2°, 21.8°, and 27.8° between the top and the middle layer, which is previously reported in the study of the twisted bilayer MoS_2 with the commensurate angles.[22]

To understand the reason of the energy broadening in the X^A exciton for the as-grown tT MoS_2 homostructures, the low-temperature PL measurements at 10K are comparably performed for samples of 14°-, 20°-, 28°-, 30°-, and 31°-tT MoS_2 homostructures. Figure 4b shows the low-temperature PL spectra of the above mentioned trilayer MoS_2 homostructures. The corresponding normalized low-temperature PL spectra are shown in Figure S8a (Supporting Information). Except for the primary A and B excitons labeled as X^A and X^B in Figure 4b, two additional peaks located at around 1.6 eV and 1.7 eV can be identified respectively in the low-temperature PL spectra from the samples of 14°-, 20°-, 28°-, 30°-, and 31°-tT MoS_2 homostructures. Based on the former research on the twisted bilayer MoS_2 homostructures, the peak projected at about 1.7 eV might be related to the defect emission (X^D),[40,44] originating from the localized excitons bound by defects such as grain boundary or vocation generated during the CVD growth procedure. This peak is further observed in LT PL spectrum from the single layer MoS_2, strongly evidencing that the peak of 1.7 eV cannot be associated with the different stacked structures and indeed caused by the defect-bound localized excitons of the monolayer in Figure S8b (Supporting Information).[40,44] As for another peak located on the left side of the defect emission peak in the low-temperature PL spectrum, this radiation recombination can be assigned to the interlayer

© 2024 Wiley-VCH GmbH

21951071, 0, Downloaded from https://onlinelibrary.wiley.com/doi/10.1002/adom.202400907 by Beijing Normal University, Wiley Online Library on [25/06/2024]. See the Terms and Conditions (https://onlinelibrary.wiley.com/terms-and-conditions) on Wiley Online Library for rules of use; OA articles are governed by the applicable Creative Commons License

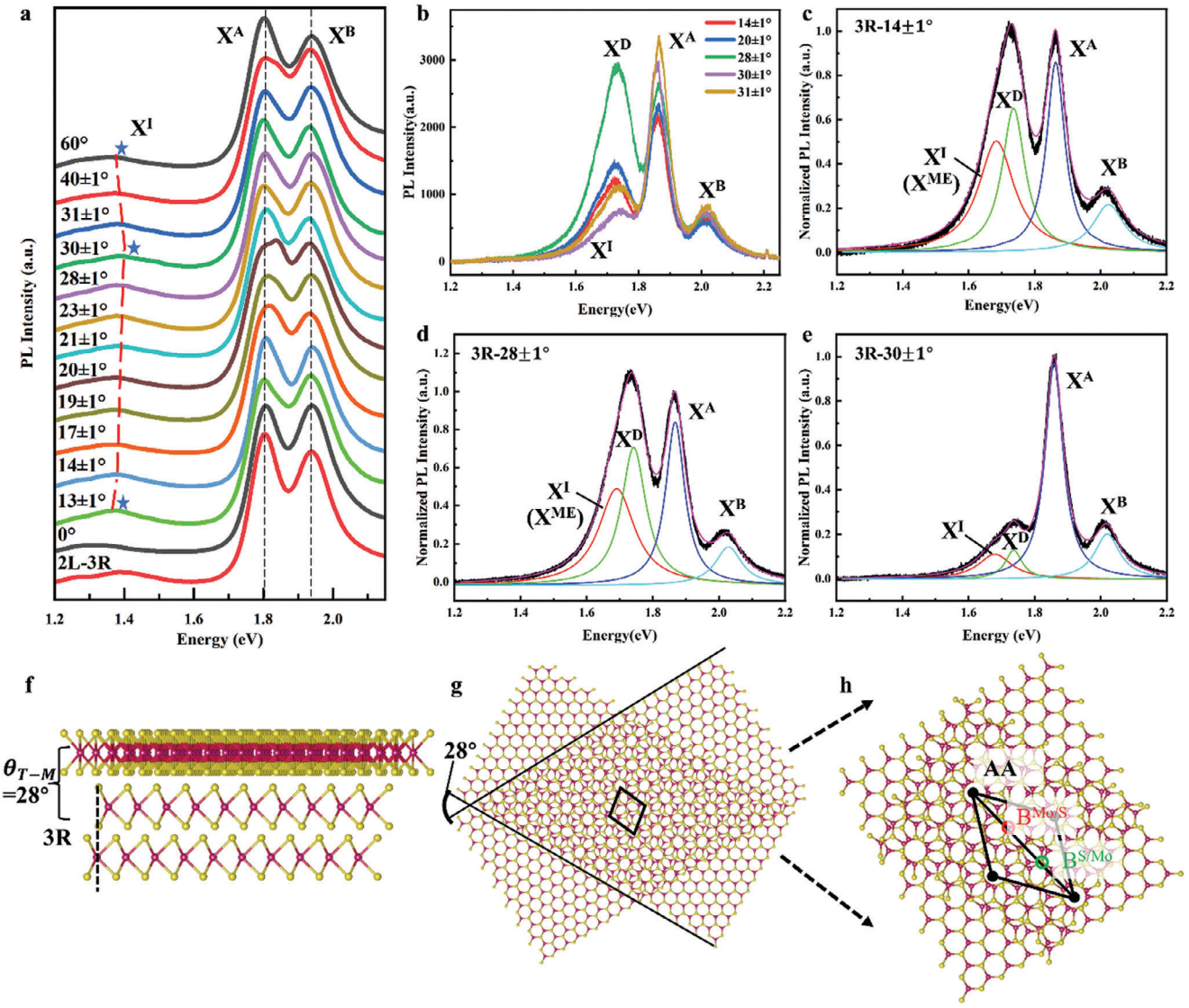

Figure 4. PL properties of top-layer tT MoS_2. a) The room-temperature PL spectra of tT MoS_2 homostructures with a 3R B-M configuration and the T-M twist angles of 0°, 13°, 14°, 28°, 30° and 31° b) Low-temperature PL spectra of 3R-14°, 3R-28°, 3R-30°, and 3R-31° tT MoS_2 at 10K. c–e) Low-temperature PL spectra of the (c) 3R-14°, (d) 3R-28°, (e) 3R-30° tT MoS_2 fitted by the Gaussian function. f) Side view of the atomic registration model of 3R-28° tT MoS_2. g) Schematic illustration of the moiré superlattice formed in a tT MoS_2 with 3R-28° in real space, and the moiré potential period labeled as a_M. h) The moiré superlattice in (g) leads to periodic modulation of the electrostatic potential of the twisted homotrilayer, showing three highlighted regions with the threefold rotational symmetry (AA, $B^{Mo/S}$, $B^{S/Mo}$), which may retain excitons and complexes of exciton.

excitons (X^I). Comparing to the energy of the X^I exciton distributed in the range of 1.367–1.388 eV for the twisted trilayer MoS_2, the energy X^I peak shift to the high energy of approximate1.6 eV. Significantly, this energy value is very close to the energy of moiré excitons, previously reported in the literature about high-angle twisted bilayer MoS_2.[22] In essence, moiré excitons belong to the interlayer excitons, which can be trapped by the periodical moiré potential formed by the large-angle commensurate superlattices in twisted bilayer MoS_2.[22]

To ensure the formation of moiré excitons, the low-temperature PL spectra are fitted by the Gaussian function as shown in Figure 4c–e and Figure S8c (Supporting Information), corresponding to the 3R-14°, 3R-28°, 3R-30°, and 3R-31° tT MoS_2 homostructures, respectively. Figure 4c shows four peaks, the A exciton (X^A = 1.867 eV), the B exciton (X^B = 2.028 eV), a defect emission peak (X^D = 1.742 eV), and the interlayer exciton (X^I = 1.689 eV), respectively. Similar phenomena can be observed in Figure 4d,e, and Figure S8c (Supporting Information). The energy values of different exciton states are listed in Table S3 (Supporting Information). We can clearly see that the intensity of interlayer moiré (X^I) is variable in the tT MoS_2 with different T-M interlayer twists, which is evidenced by the ratio between the X^I and X^A (namely, $R_{I/A}$). The value of $R_{I/A}$ is changeable and gradually decreased from 0.604, 0.583, 0.182, and 0.118 for the 3R-14°, 3R-28°, 3R-30°, 3R-31° tT MoS_2 samples. This means that interlayer excitons can be bound by the moiré potential, which only

© 2024 Wiley-VCH GmbH

21951071, 0, Downloaded from https://onlinelibrary.wiley.com/doi/10.1002/adom.202400907 by Beijing Normal University, Wiley Online Library on [25/06/2024]. See the Terms and Conditions (https://onlinelibrary.wiley.com/terms-and-conditions) on Wiley Online Library for rules of use; OA articles are governed by the applicable Creative Commons License

happens on the commensurate superlattices caused by the commensurate large twist angles such as 13.2° and 27.8°. In this case, two T-M twist angles of 14° and 28° are pretty close to the above two commensurate angles. The detailed stacking structures of twisted trilayer MoS_2 are shown in Figure 4f–h. It tells that there are high symmetric atom stacking locations of AA, AB and BA in the moiré superlattices (Figure 4h), which induces the moiré potential larger than that of the incommensurate superlattices from the 3R-30° and 3R-31° tT MoS_2 homostructures. Accordingly, the interlayer excitons, named as moiré excitons, can be trapped in these high symmetric dots, resulting in the energy shift and increased intensity in LT PL spectra.

3. Conclusion

In conclusion, high-quality tT MoS_2 homostructures with the twisted top-layer were successfully fabricated via a NaCl-assisted CVD method. The evolution of the interlayer coupling in twisted trilayer MoS_2 was investigated by Raman and PL spectra. Raman and PL results show the trilayer interlayer interaction are sensitively dependent on the commensurate twist angles of 14° and 28°. Moiré excitons, were observed in the top-layer twisted MoS_2 trilayer with T-M twists of 14° and 28° and enhanced in the top-layer twisted trilayer MoS_2 homostructures with special twists of approximate 28°, which originates from the interlayer excitons trapped by the periodical moiré potential. The present work demonstrates that the trilayer homostructures tuned by interlayer twists can be an ideal system to tune the energy band structures and exciton properties for their potential applications in the nano-optical electronics.

4. Experimental Section

CVD Growth of the Top-Layer Twisted Trilayer (tT) MoS_2 Structures: The top-layer twisted trilayer MoS_2 patterns were grown on 300-nm-thick SiO_2/Si substrate by a NaCl-assisted CVD method, with crystal sizes ranging from 10 to 20 µm. During CVD growth process, MoO_3 powder (99.9%, 5 mg, Alfa Aesar) and sulfer powder (99.95%, 50 mg, Alfa Aesar) were placed on different temperature zones, meanwhile, the SiO_2/Si substrate was upside down set away from the MoO_3 precursor with the distance of 1 cm. Here, the argon gas was used as the carrier gas with the gas flow rate ranging from 50 to 100 sccm for the growth of twisted trilayer MoS_2 crystals. The furnace temperature was ramped from 30 °C to 700 °C for 20 min, the reaction time was kept for 10 min under atmospheric pressure. The temperature of the MoO_3 and sulfur precursor was set at 800 °C and 130 °C, respectively. After finishing the MoS_2 growth, the CVD system was cooled down to room temperature without any assistance.

Measurement of Raman and PL Spectroscopy: Low frequency and high frequency Raman spectra were measured at room temperature using a micro-Raman system (Horiba, LabRAM HR Evolution NANO) equipped with 1800 lines mm^{-1} gratings with laser energy of 2.33 eV (532 nm). A ×100 objective lens (numerical aperture = 0.90) was used to focus the laser beam to a spot ≈1 µm in diameter on the sample surface.

PL and LT PL spectra were recorded with a confocal Raman microscope (InVia, Renishaw U.K.) at room temperature with a 532 nm He-Cd laser as the excitation source. The 100 lines mm^{-1} grating is used in the PL measurements.

Supporting Information

Supporting Information is available from the Wiley Online Library or from the author.

Acknowledgements

R.F.D. acknowledges support from the National Natural Science Foundation of China (grant nos. 11974048, 12074053, 62174179, and 92265110).

Conflict of Interest

The authors declare no conflict of interest.

Author Contributions

Y.L.L., J.Z., and T.T.Z. contributed equally to this work. R.F.D. and Y.L.L. conceived the present experiments. Y.L.L. and J.Z. prepared the samples of MoS_2 trilayer on SiO_2/Si substrates. Y.L.L, M.J.Z, and S.S.C. carried out the Raman spectrum measurements. J.Z., Y.L.L., Z.H.Z., W.F.Z., and N.L. performed the PL measurements. R.F.D., Y.L.L., J.Z., and T.T.Z. analyzed the experimental data. R.F.D. completed writing the text. All authors discussed the results and commented on the manuscript.

Data Availability Statement

The data that support the findings of this study are openly available in 3900 at https://doi.org/10.1002/adom.202400907, reference number 44.

Keywords

Interlayer twist, Moire exciton, Photoluminescence, Transition metal dichalcogenides, Trilayer homostructures

Received: April 7, 2024
Revised: June 3, 2024
Published online:

[1] Y. Shimazaki, I. Schwartz, K. Watanabe, T. Taniguchi, M. Kroner, A. Imamoğlu, *Nature* **2020**, *580*, 472.
[2] L. Wang, E.-M. Shih, A. Ghiotto, L. Xian, D. A. Rhodes, C. Tan, M. Claassen, D. M. Kennes, Y. Bai, B. Kim, K. Watanabe, T. Taniguchi, X. Zhu, J. Hone, A. Rubio, A. N. Pasupathy, C. R. Dean, *Nat. Mater.* **2020**, *19*, 472.
[3] Y. Cao, V. Fatemi, A. Demir, S. Fang, S. L. Tomarken, J. Y. Luo, J. D. Sanchez-Yamagishi, K. Watanabe, T. Taniguchi, E. Kaxiras, R. C. Ashoori, P. Jarillo-Herrero, *Nature* **2018**, *556*, 861.
[4] Y. Cao, V. Fatemi, S. Fang, K. Watanabe, T. Taniguchi, E. Kaxiras, P. Jarillo-Herrero, *Nature* **2018**, *556*, 43.
[5] Y. Cao, J. M. Park, K. Watanabe, T. Taniguchi, P. Jarillo-Herrero, *Nature* **2021**, *595*, 526.
[6] X. Lu, P. Stepanov, W. Yang, M. Xie, M. A. Aamir, I. Das, C. Urgell, K. Watanabe, T. Taniguchi, G. Zhang, A. Bachtold, A. H. Macdonald, D. K. Efetov, *Nature* **2019**, *574*, 653.
[7] J. M. Park, Y. Cao, K. Watanabe, T. Taniguchi, P. Jarillo-Herrero, *Nature* **2021**, *590*, 249.
[8] S. Tao, X. Zhang, J. Zhu, P. He, S. A. Yang, Y. Lu, S. Wei, *J. Am. Chem. Soc.* **2022**, *144*, 3949.
[9] D. Chen, Z. Lian, X. Huang, Y. Su, M. Rashetnia, L. Yan, M. Blei, T. Taniguchi, K. Watanabe, S. Tongay, Z. Wang, C. Zhang, Y.-T. Cui, S.-F. Shi, *Nat. Commun.* **2022**, *13*, 4810.
[10] S. Venkateswarlu, A. Honecker, G. Trambly De Laissardière, *Phys. Rev. B* **2020**, *102*, 081103.
[11] F. Wu, T. Lovorn, E. Tutuc, A. H. Macdonald, *Phys. Rev. Lett.* **2018**, *121*, 26402.

© 2024 Wiley-VCH GmbH

21951071, 0, Downloaded from https://onlinelibrary.wiley.com/doi/10.1002/adom.202400907 by Beijing Normal University, Wiley Online Library on [25/06/2024]. See the Terms and Conditions (https://onlinelibrary.wiley.com/terms-and-conditions) on Wiley Online Library for rules of use; OA articles are governed by the applicable Creative Commons License

[12] X. Zhao, J. Qiao, S. M. Chan, J. Li, J. Dan, S. Ning, W. Zhou, S. Y. Quek, S. J. Pennycook, K. P. Loh, *Nano Lett.* **2021**, *21*, 3262.
[13] Z. Zhang, Y. Wang, K. Watanabe, T. Taniguchi, K. Ueno, E. Tutuc, B. J. Leroy, *Nat. Phys.* **2020**, *16*, 1093.
[14] M. Liao, Z. Wei, L. Du, Q. Wang, J. Tang, H. Yu, F. Wu, J. Zhao, X. Xu, B. Han, K. Liu, P. Gao, T. Polcar, Z. Sun, D. Shi, R. Yang, G. Zhang, *Nat. Commun.* **2020**, *11*, 2153.
[15] E. Li, J. Hu, X. Feng, Z. Zhou, L. An, K. T. Law, N. Wang, N. Lin, *Nat. Commun.* **2021**, *12*, 5601.
[16] Y. Xiao, J. Liu, L. Fu, *Matter* **2020**, *3*, 1142.
[17] L. J. Mcgilly, A. Kerelsky, N. R. Finney, K. Shapovalov, E.-M. Shih, A. Ghiotto, Y. Zeng, S. L. Moore, W. Wu, Y. Bai, K. Watanabe, T. Taniguchi, M. Stengel, L. Zhou, J. Hone, X. Zhu, D. N. Basov, C. Dean, C. E. Dreyer, A. N. Pasupathy, *Nat. Nanotechnol.* **2020**, *15*, 580.
[18] H. Li, S. Li, M. H. Naik, J. Xie, X. Li, J. Wang, E. Regan, D. Wang, W. Zhao, S. Zhao, S. Kahn, K. Yumigeta, M. Blei, T. Taniguchi, K. Watanabe, S. Tongay, A. Zettl, S. G. Louie, F. Wang, M. F. Crommie, *Nat. Mater.* **2021**, *20*, 945.
[19] L. Rademake, *Phys. Rev. B* **2022**, *105*, 195428.
[20] K. Shinokita, Y. Miyauchi, K. Watanabe, T. Taniguchi, K. Matsuda, *Nano Lett.* **2021**, *21*, 5938.
[21] E. Barré, O. Karni, E. Liu, A. L. O'Beirne, X. Chen, H. B. Ribeiro, L. Yu, B. Kim, K. Watanabe, T. Taniguchi, *Science* **2022**, *376*, 406.
[22] X. Zhao, J. Qiao, X. Zhou, H. Chen, J. Y. Tan, H. Yu, S. M. Chan, J. Li, H. Zhang, J. Zhou, J. Dan, Z. Liu, W. Zhou, Z. Liu, B. Peng, L. Deng, S. J. Pennycook, S. Y. Quek, K. P. Loh, *Nano Lett.* **2022**, *22*, 203.
[23] D. Huang, J. Choi, C.-K. Shih, X. Li, *Nat. Nanotechnol.* **2022**, *17*, 227.
[24] Q. Shi, E.-M. Shih, D. Rhodes, B. Kim, K. Barmak, K. Watanabe, T. Taniguchi, Z. Papić, D. A. Abanin, J. Hone, C. R. Dean, *Nat. Nanotechnol.* **2022**, *17*, 577.
[25] J. Yan, J. Xia, X. Wang, L. Liu, J.-L. Kuo, B. K. Tay, S. Chen, W. Zhou, Z. Liu, Z. X. Shen, *Nano Lett.* **2015**, *15*, 8155.
[26] E. C. Regan, D. Wang, E. Y. Paik, Y. Zeng, L. Zhang, J. Zhu, A. H. Macdonald, H. Deng, F. Wang, *Nat. Rev. Mater.* **2022**, 778.
[27] D. Schmitt, J. P. Bange, W. Bennecke, A. Almutairi, G. Meneghini, K. Watanabe, T. Taniguchi, D. Steil, D. R. Luke, R. T. Weitz, S. Steil, G. S. M. Jansen, S. Brem, E. Malic, S. Hofmann, M. Reutzel, S. Mathias, *Nature* **2022**, *608*, 499.
[28] C. Jin, E. C. Regan, A. Yan, M. Iqbal Bakti Utama, D. Wang, S. Zhao, Y. Qin, S. Yang, Z. Zheng, S. Shi, K. Watanabe, T. Taniguchi, S. Tongay, A. Zettl, F. Wang, *Nature* **2019**, *567*, 76.
[29] K. Tran, G. Moody, F. Wu, X. Lu, J. Choi, K. Kim, A. Rai, D. A. Sanchez, J. Quan, A. Singh, J. Embley, A. Zepeda, M. Campbell, T. Autry, T. Taniguchi, K. Watanabe, N. Lu, S. K. Banerjee, K. L. Silverman, S. Kim, E. Tutuc, L. Yang, A. H. Macdonald, X. Li, *Nature* **2019**, *567*, 71.
[30] M. H. Naik, E. C. Regan, Z. Zhang, Y.-H. Chan, Z. Li, D. Wang, Y. Yoon, C. S. Ong, W. Zhao, S. Zhao, M. I. B. Utama, B. Gao, X. Wei, M. Sayyad, K. Yumigeta, K. Watanabe, T. Taniguchi, S. Tongay, F. H. Da Jornada, F. Wang, S. G. Louie, *Nature* **2022**, *609*, 52.
[31] T. I. Andersen, G. Scuri, A. Sushko, K. De Greve, J. Sung, Y. Zhou, D. S. Wild, R. J. Gelly, H. Heo, D. Bérubé, A. Y. Joe, L. A. Jauregui, K. Watanabe, T. Taniguchi, P. Kim, H. Park, M. D. Lukin, *Nat. Mater.* **2021**, *20*, 480.
[32] S. Xie, B. D. Faeth, Y. Tang, L. Li, E. Gerber, C. T. Parzyck, D. Chowdhury, Y. H. Zhang, C. Jozwiak, A. Bostwick, *Sci. Adv.* **2022**, *8*, 1911.
[33] B. Wu, H. Zheng, S. Li, J. Ding, J. He, Y. Zeng, K. Chen, Z. Liu, S. Chen, A. Pan, Y. Liu, *Light: Sci. Appl.* **2022**, *11*, 166.
[34] S. Chen, M. He, Y.-H. Zhang, V. Hsieh, Z. Fei, K. Watanabe, T. Taniguchi, D. H. Cobden, X. Xu, C. R. Dean, M. Yankowitz, *Nat. Phys.* **2020**, *17*, 374.
[35] X. Luo, X. Lu, C. Cong, T. Yu, Q. Xiong, S. Ying Quek, *Sci. Rep.* **2015**, *5*, 14565.
[36] A. A. Puretzky, L. Liang, X. Li, K. Xiao, B. G. Sumpter, V. Meunier, D. B. Geohegan, *ACS Nano* **2016**, *10*, 2736.
[37] S. Huang, L. Liang, X. Ling, A. A. Puretzky, D. B. Geohegan, B. G. Sumpter, J. Kong, V. Meunier, M. S. Dresselhaus, *Nano Lett.* **2016**, *16*, 1435.
[38] A. A. Puretzky, L. Liang, X. F. Li, K. Xiao, K. Wang, M. Mahjouri-Samani, L. Basile, J. C. Idrobo, B. G. Sumpter, V. Meunier, D. B. Geohegan, *ACS Nano* **2015**, *9*, 6333.
[39] K. Kim, J.-U. Lee, D. Nam, H. Cheong, *ACS Nano* **2016**, *10*, 8113.
[40] Y. Wang, L. Deng, Q. Wei, Y. Wan, Z. Liu, X. Lu, Y. Li, L. Bi, L. Zhang, H. Lu, H. Chen, P. Zhou, L. Zhang, Y. Cheng, X. Zhao, Y. Ye, W. Huang, S. J. Pennycook, K. P. Loh, B. Peng, *Nano Lett.* **2020**, *20*, 2129.
[41] J. Quan, L. Linhart, M.-L. Lin, D. Lee, J. Zhu, C.-Y. Wang, W.-T. Hsu, J. Choi, J. Embley, C. Young, T. Taniguchi, K. Watanabe, C.-K. Shih, K. Lai, A. H. Macdonald, P.-H. Tan, F. Libisch, X. Li, *Nat. Mater.* **2021**, *20*, 1100.
[42] M.-L. Lin, Q.-H. Tan, J.-B. Wu, X.-S. Chen, J.-H. Wang, Y.-H. Pan, X. Zhang, X. Cong, J. Zhang, W. Ji, P.-A. Hu, K.-H. Liu, P.-H. Tan, *ACS Nano* **2018**, *12*, 8770.
[43] K. F. Mak, C. Lee, J. Hone, J. Shan, T. F. Heinz, *Phys. Rev. Lett.* **2010**, *13*, 136805.
[44] B. Schuler, D. Y. Qiu, S. Refaely-Abramson, C. Kastl, C. T. Chen, S. Barja, R. J. Koch, D. F. Ogletree, S. Aloni, A. M. Schwartzberg, J. B. Neaton, S. G. Louie, A. Weber-Bargioni, *Phys. Rev. Lett.* **2019**, *123*, 076801.

© 2024 Wiley-VCH GmbH

21951071, 0, Downloaded from https://onlinelibrary.wiley.com/doi/10.1002/adom.202400907 by Beijing Normal University, Wiley Online Library on [25/06/2024]. See the Terms and Conditions (https://onlinelibrary.wiley.com/terms-and-conditions) on Wiley Online Library for rules of use; OA articles are governed by the applicable Creative Commons License